ORIGINAL PAPER

Solid-State Deposit-Induced Corrosion of a Second-Generation Nickel-Based Superalloy Caused by CaO and CaSO$_4$ Deposits

Patrick T. Brennan[1,3] ⓘ **· Doug Konitzer**[2,3] **· Michael Brennan**[2,4] **· Brian Gleeson**[3]

Abstract
The goal of this research project was to provide a fundamental understanding of CaO-and CaSO$_4$-induced corrosion in second-generation Ni-based single-crystal superalloys and to develop a lab-scale test procedure, which accurately replicates corrosion observed in field-exposed components. Secondary and transmission electron microanalyses were used to characterize the corrosion of field-exposed components taken from commercial aviation turbines. It was found that the field-exposed components had been attacked by internal oxidation-sulfidation. Isothermal laboratory-scale experiments at 900 and 1150 °C in air were conducted on superalloy coupons deposited with either CaO or CaSO$_4$ to assess the extents and modes of solid-state corrosion caused by either deposit. A novel bi-thermal test procedure was then developed which effectively replicated the internal oxidation-sulfidation found in the field-exposed components. It was determined that compositional and microstructural changes to the alloy subsurface caused by CaSO$_4$-induced corrosion at elevated temperatures made the alloy susceptible to internal oxidation at lower temperatures.

Keywords Corrosion · Gas turbine · Internal oxidation · Sulfidation

✉ Patrick T. Brennan
    patrick.t.brennan@ge.com

[1] Present Address: GE Research, Niskayuna, NY, USA

[2] GE Aviation, Cincinnati, OH, USA

[3] Present Address: University of Pittsburgh, Pittsburgh, PA, USA

[4] Present Address: Blue Origin, Seattle, WA, USA

Introduction

Accelerated oxidation and sulfidation of structural metals caused by sulfate deposits affect materials used in high-temperature applications such as power generation and naval and air propulsion [1–4]. Due to the impact of deposit-induced corrosion across a variety of applications, there is a large body of research on the influences of temperature, atmosphere, alloy composition, and deposit composition on the modes and extents of corrosion [5]. However, for the case of corrosion in aircraft engines, most of the past research examined corrosion induced by Na_2SO_4 deposits. This has resulted in a gap in knowledge specific to modes of corrosion in aircraft engines caused by deposits of different compositions.

Recent publications [6, 7] have reported internal oxidation and sulfidation attack in high-pressure turbine airfoils and shrouds of aircraft engines in the presence of calcium-rich deposits. While modes of corrosion associated with calcium-rich deposits have been investigated for applications in electrical power generation [8–12], information on related mechanisms of corrosion for nickel-based superalloys used in high-pressure turbines remains sparse.

Thermodynamic calculations of the stability of calcium-containing deposits reveal that either CaO or $CaSO_4$ may be stable within the high-pressure turbine environment [13]. For example, the transition temperature between CaO and $CaSO_4$ stability is about 1100 °C in a 1 atm 10 ppm $SO_2 + O_2$ environment, with $CaSO_4$ being the stable phase below this temperature. Because of this borderline stability, both CaO- and $CaSO_4$-induced modes of corrosion of nickel-based superalloys need to be studied.

This paper presents the results of work conducted to identify and reproduce the mechanisms by which deposits rich in Ca, O, and S can cause internal oxidation and sulfidation in single-crystal nickel-based superalloys used in the high-pressure turbine of aircraft engines. In this paper, corroded field-exposed components with Ca, O, and S-rich deposits were characterized by SEM and TEM analyses. Modes of CaO- and $CaSO_4$-induced corrosion were then investigated using laboratory-scale experiments. Finally, a laboratory-scale testing procedure was developed to accurately replicate the corrosion observed in the field-exposed components.

Table 1 Nominal composition of Rene N500 [14]

Rene N500	Ni	Co	Cr	Al	Ta	W	Mo	C	B	Hf	Y
at%	Bal	7.6	6.9	13.9	2.1	2	0.9	0.2	0.02	0.05	0.02
wt%	Bal	7.6	6.1	6.3	6.4	6.2	1.5	0.04	0.004	0.15	0.03

Experimental Procedures

Field-exposed Samples

The characterization of corroded field-exposed components was done by examining three Rene N500 samples from different engines provided by GE Aviation. Each sample was taken from the same type of engine component. The nominal composition of Rene N500 is presented in Table 1. Each component was cross-sectioned at locations where corrosion was evident, mounted in epoxy resin, and prepared for microscopy using a series of SiC paper and then a diamond-based polishing solution to a final finish of 0.25 µm. Oil or alcohol-based solutions were used during cutting, grinding, and polishing to retain any water-soluble corrosion products. The samples were cleaned in ethanol and then sputter-coated with a thin film of palladium before electron microscopy. The corrosion product was characterized using scanning electron microscopy (SEM) and, in certain cases, transmission electron microscopy (TEM) of samples produced by focused ion beam (FIB) lift-out from areas of interest identified during SEM analysis. The composition and structure of the corrosion product formed on the components were found to be complex, so most phase identification in this work was made through interpreting semi-quantitative EDS analysis in conjunction with consideration of the thermodynamic stability of potential products. Additionally, energy electron loss spectroscopy (EELS) was used near the internal oxidation front in one of the TEM sections to look for the presence of sulfur dissolved in the alloy.

Lab Samples

Rectangular single-crystal N500 coupons ($25 \times 12.5 \times 3$ mm) provided by GE Aviation in the as-cast condition were prepared for furnace testing by grinding the flat surfaces to a P1200-grit finish using SiC paper followed by ultrasonic cleaning in pure ethanol. CaO or $CaSO_4$ was applied to the largest face of the clean coupons by wetting that face with ethanol and placing the desired mass of deposit into the ethanol bead. The surface tension of the ethanol bead ensured an even distribution of the deposit on the surface. The coupons were heated on a hot plate set at about 150 °C to evaporate the ethanol. The coupon was then weighed using an analytical balance accurate to ± 0.01 mg.

The CaO-alloy interactions were investigated by exposing coupons deposited with $2.5 \pm 0.5 \frac{mg}{cm^2}$ of 99.9% purity CaO for either 100 h at 900 °C or 24 h at 1150 °C in air. Owing to the inertia of initial experiments, the $CaSO_4$-alloy interactions were investigated by using a greater deposit amount. Specifically, coupons were deposited with $20 \pm 1 \frac{mg}{cm^2}$ of 99% purity $CaSO_4$-anhydrous and then exposed for either 100 h at 900 °C or 0.5, 1, 8, or 24 h at 1150 °C in air. Additionally, $CaSO_4$-Al_2O_3 interactions at 1150 °C were investigated by exposing bulk 99.8% purity Al_2O_3 deposited with $20 \pm 1 \frac{mg}{cm^2}$ of $CaSO_4$-anhydrous for 0.5, 8, or 24 h at 1150 °C in air. All laboratory-scale exposures were conducted using a horizontal tube furnace for which air was flowed through the furnace tube at a rate of $50 \frac{mL}{min}$. The source of air for all of

the experiments in this work was compressed in a standard gas cylinder (UN1002). Using a custom endcap and sample carrier configuration, all coupons were directly loaded into the pre-heated furnace under the controlled atmosphere. The furnace tubes used were 99.8% aluminum oxide with an inner diameter of 4.45 cm.

The findings from the isothermal experiments with CaO and $CaSO_4$ deposit led to the development of two additional experiments. The first additional experiment was a "bi-thermal" test developed to investigate how thermal profile and atmospheric steam influence the modes of corrosion caused by CaO and $CaSO_4$ deposits. Coupons with $20 \pm 1 \frac{mg}{cm^2}$ of $CaSO_4$ deposit or $8.25 \pm 0.5 \frac{mg}{cm^2}$ of CaO deposit (an equimolar mass of $CaSO_4$ and CaO deposit) were exposed to a thermal profile that had an initial 8-h exposure at 1150 °C followed by cooling to 871 °C and holding for 60 h or 96 h. The atmosphere for these exposures was air or air + 30% steam. A gas mixture of air + 30% steam was achieved by bubbling the compressed air through deionized water heated to 72 °C and then through a condenser kept at 70 °C via flowing heated water from a separate bath. In accordance with a saturated steam table [15], the vapor pressure of water is about 0.3 atm at 70 °C.

The second additional experiment was developed to investigate the role that subsurface sulfidation plays on the mode of $CaSO_4$-induced corrosion during bi-thermal testing. Two coupons with $20 \frac{mg}{cm^2}$ of $CaSO_4$ deposit were exposed for 8 h at 1150 °C in air + 30% steam. Following the initial exposure, the surfaces of both coupons were grit blasted with alumina to remove any external reaction product and ensure that the surfaces would be exposed to the atmosphere. One of the coupons was given a desulfurization treatment of 24 h exposure at 1000 °C in Ar + 5% H_2. After the desulfurization, both the test and control coupons were subjected to the 60-h second stage exposure at 871 °C in air + 30% steam.

All coupons were characterized after exposure by cross-sectional imaging using electron microscopy techniques. Samples were prepared for microscopy using the same procedures described for the field exposed samples. Most coupons were cross-sectioned twice prior to grinding and polishing to ensure that three unique regions could be characterized from each coupon. Additionally, X-ray diffraction (XRD) was used to identify reaction products that formed within $CaSO_4$-Al_2O_3 couples. Prior to XRD, the remnant $CaSO_4$ deposit was removed from the surface of the Al_2O_3 by washing it with water, lightly abrading the surface with P1200 SiC paper, and then leaving the coupon in an ultrasonic bath with water for an hour.

Results and Discussion

Characterization of Corrosion Observed in the Field-exposed Components

Cross-sectional SEM micrographs of the reaction product are presented in Fig. 1. The three field components were of the same type and the images/analyses were taken in similar locations on the three components. The reaction product was similar for all three sections. The corrosion consisted of an external Ni-rich oxide layer
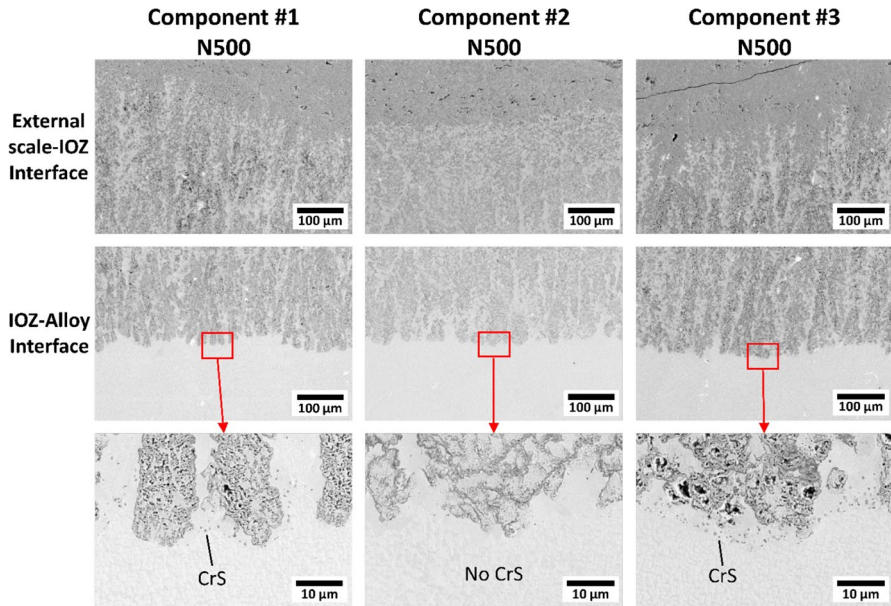
Fig. 1 Cross-sectional SEM micrographs of components #1, #2, and #3. The top row of images shows the interface between the external NiO and the internal oxidation zone, the middle row of images shows the internal oxidation front, and the bottom row shows high magnification images of the internal oxidation front

above an internal oxidation zone (IOZ). The IOZ consisted of dendrite-like intrusions of coarse Al- and Cr-rich oxide precipitates and γ-Ni. The external layer of Ni-rich oxide was intermixed with phases rich in Al and Cr. This suggests that at least the inner portion of the external product was once part of the internal oxidation zone that had fully oxidized. A fine distribution of CrS precipitates was present

Fig. 2 SEM image marking the location where the FIB lift-out was taken near the external oxide layer (red box)
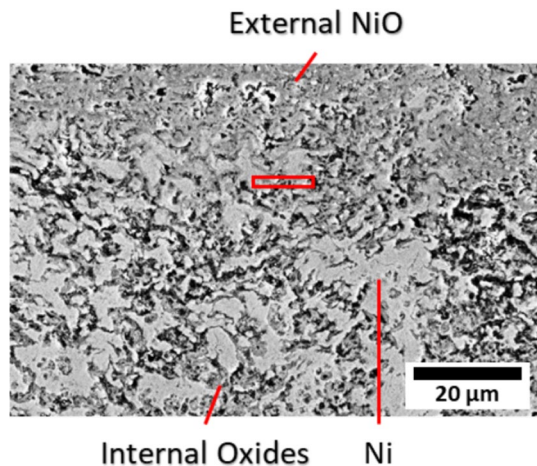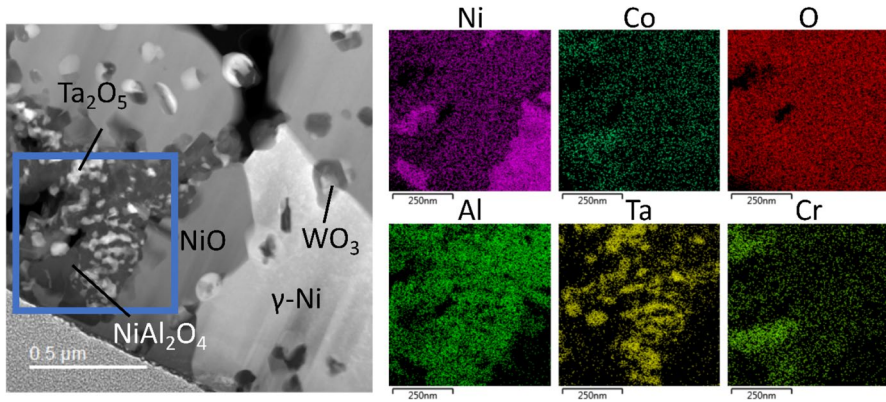
Fig. 3 High magnification of the IOZ near the external oxide layer. EDS mapping was done in the blue box. The chemical stoichiometry was inferred based on the semi-quantitative EDS performed during SEM and relevant thermodynamic stability

in the γ′-denuded zone ahead of the internal oxidation front in components #1 and #3 but was absent in component #2 (Fig. 1). The development of the IOZ was of particular interest in this study because its significant thickness and morphology are not typical of what has been reported in previously published laboratory-scale test results [8–12]. Remnant deposit was found on component #1. EDS analysis of the deposit revealed that the deposit consisted primarily of Ca, O, and S with a smaller amount of Mg. This suggested that the internal oxidation was linked to calcium-rich deposit-induced attack.

The chemistry of the internal oxide product near the interface between the IOZ and the external Ni-rich product was determined via TEM analysis of FIB lift-outs from locations of interest in component #2 (Fig. 2). The corresponding EDS
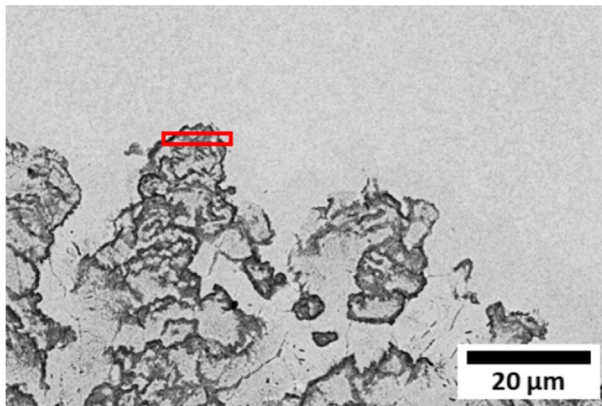

Fig. 4 SEM image marking the location where the FIB lift-out was taken near the internal oxidation front (red box)
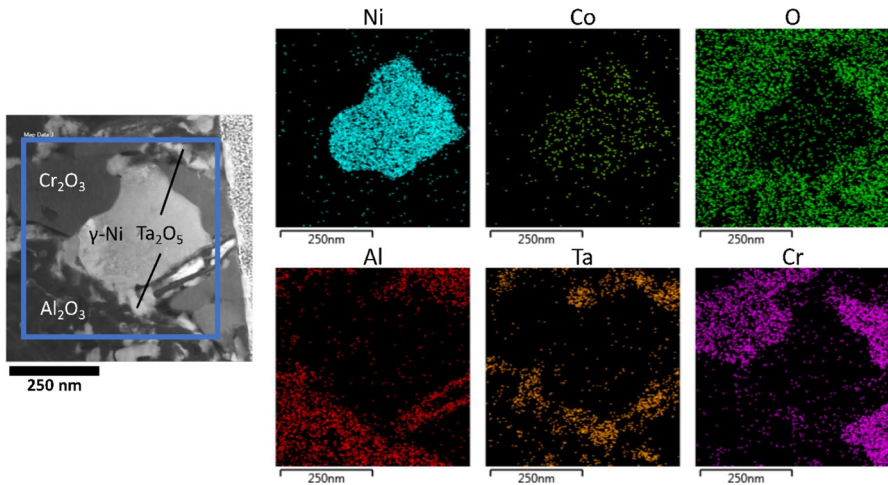
Fig. 5 High magnification of an area near the internal oxidation front. EDS mapping was done in the blue box. The chemical stoichiometry was inferred based on the semi-quantitative EDS performed during SEM and relevant thermodynamic stability

analysis of the area is summarized in Fig. 3. The internal oxide product near the IOZ-external product interface was comprised of γ-Ni that was depleted of solute elements Al and Cr and a mix of several oxides, primarily NiO and $NiAl_2O_4$ spinel. Additionally, tantalum oxide was present and intermixed with the $NiAl_2O_4$ and WO_3 particles had formed at Ni-NiO interfaces.

A region of the sample lifted from the internal oxidation front is shown in Fig. 4 and the corresponding EDS analysis of the area is shown in Fig. 5. Based on the compositions measured by EDS, Al_2O_3, Cr_2O_3, Ta_2O_5, and γ-Ni islands were the inferred constituents of the internal oxide product at the internal oxidation front. Further, the γ-Ni islands were significantly depleted in Al, Cr and Ta, in accordance with their selective oxidation at the low oxygen potentials at the internal oxidation front.
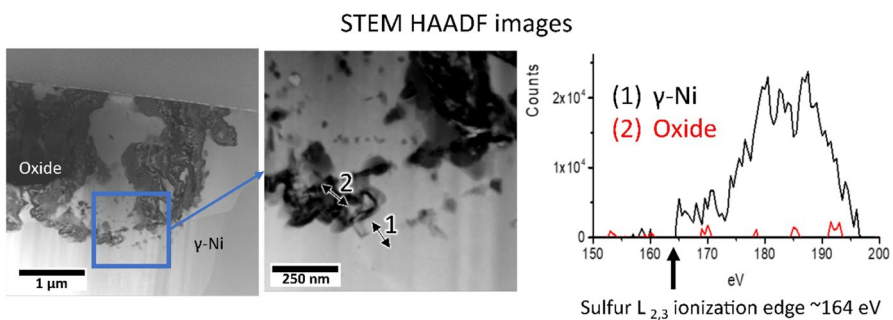

Fig. 6 EELS analysis detects sulfur in the γ′-denuded zone ahead of the internal oxidation front, Line 1, but no S present in the oxide phase, Line 2

In addition to identifying the constituents of the internal oxide product, EELS analysis was used to determine if sulfur was present in the γ′-denuded zone ahead of the internal oxidation front in component #2. All three components examined exhibited a very similar corrosion morphology, but only components #1 and #3 had a fine distribution of CrS particles ahead of the internal oxidation front. The absence of CrS particles in component #2 raised questions about the role that sulfur plays in the internal oxidation process. Micrographs of the area examined and the results of the EELS analysis from line scans 1 (γ-Ni) and 2 (oxide precipitate) are shown in Fig. 6. The results show that there was no sulfur present in the oxide precipitates but that there was sulfur in the γ-Ni at the internal oxidation front. Thus, though the level of sulfur in the alloy ahead of the internal oxidation front was insufficient to stabilize CrS formation, at least in the region analyzed, sulfur was indeed present at the internal oxidation front in component #2.

The phases present through the depth of the IOZ were consistent with what would be expected for internal oxidation based on the thermodynamic stability of the relevant oxides (Fig. 7). In the IOZ near the interface with the external NiO-rich product, the P_{O_2} was sufficient to stabilize WO_3, NiO and $Ni(Al,Cr)_2O_4$ formation. Near the internal oxidation front, the oxygen chemical potential must have been low as it was only sufficient to form the most stable oxides, Al_2O_3, Ta_2O_5, and Cr_2O_3. Ahead of the internal oxidation front where the P_{O_2} is lowest, there is sulfur enrichment that typically manifests as CrS precipitates.

The mechanisms by which Ca-containing deposits may induce internal oxidation in second-generation Ni-based superalloys are investigated in the following section of this paper by exposing coupons with CaO and $CaSO_4$ deposits. Particular attention was paid to the extent of Al and Cr depletion (two elements critical to the establishment of a protective Al_2O_3 scale on Ni-based alloys [16]) that developed in the alloy subsurface.
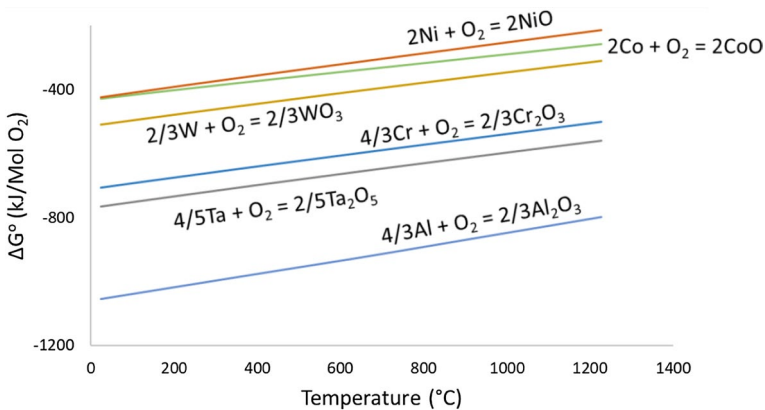

Fig. 7 Thermodynamic stability of relevant oxide phases [13]. The most stable oxide in this diagram is Al_2O_3 and the least stable is NiO
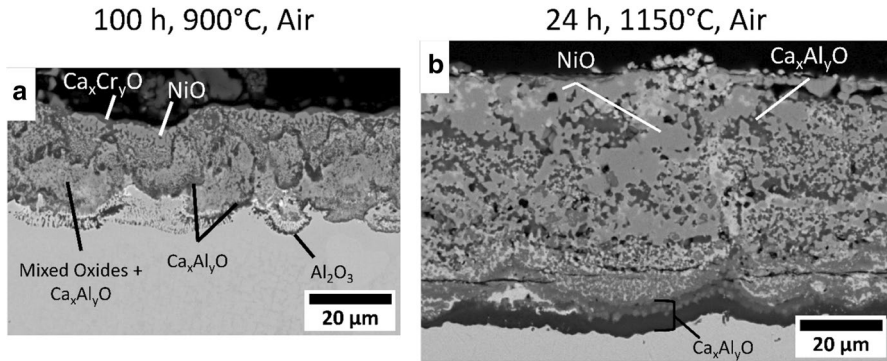
Fig. 8 Reaction product formed on substrate with CaO deposit after 100 h at 900 °C (**a**) and 24 h at 1150 °C (**b**)

Interactions Between CaO or CaSO$_4$ Deposits and Substrate During Isothermal Exposure in Air

CaO Interaction

Figure 8 presents representative cross-sectional images of the reaction product formed on coupons deposited with $2.5 \pm 0.5 \frac{mg}{cm^2}$ of CaO and exposed to air for either 100 h at 900 °C or 24 h at 1150 °C. The coupon exposed at 900 °C formed an adherent mixed oxide plus calcium-aluminate reaction product. Al$_2$O$_3$ was the primary phase formed at the oxidation front and the bulk of the external reaction product consisted of mixed Ni, Co, Al, and Cr oxides with bands of calcium aluminate. The outer portion of the product consisted of calcium chromate with embedded particles of (Ni, Co)O. Local areas showed that limited internal oxidation of aluminum had occurred.

For the alloys exposed at 1150 °C, relatively thick layers of calcium aluminates were present at the oxidation front. EDS analysis of these layers revealed that they consisted primarily of two calcium-aluminate stoichiometries, inferred to be a
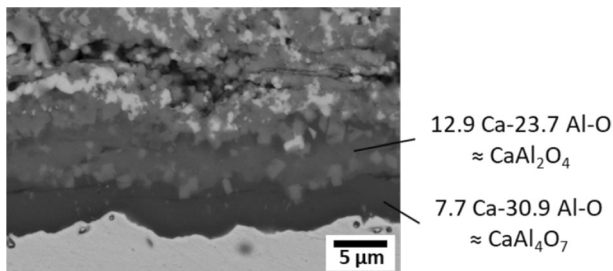

Fig. 9 EDS measurements of the Ca$_x$Al$_y$O formed on coupons exposed at 1150 C for 24 h with CaO deposit

$CaAl_4O_7$ layer and a $CaAl_2O_4$ layer, as shown in Fig. 9. The remainder of the product consisted of dense $(Ni,Co)O$ surrounding darker islands of calcium aluminate. No calcium chromate was observed in the CaO-induced reaction product formed at 1150 °C. The arrangement of the calcium aluminate layers is consistent with the results reported by Gheno et al. [12].

The mode of CaO-induced corrosion observed in these experiments is in agreement with previously published results for CaO-induced corrosion of nickel-based alloys [11, 12, 17]. CaO deposits cause accelerated oxidation by reacting with Al_2O_3 and Cr_2O_3 during the initial stages of exposure. The reaction then continues through the inward diffusion of Ca and O through the reaction product which consumes protective oxides and forms non-protective calcium aluminates and calcium chromates. The failure to establish a protective oxide scale results in broad-front, rapid oxidation of the alloy. While internal oxidation did occur locally in the coupons exposed at 900 °C, breakaway internal oxidation similar to the field-exposed components was not observed in the present experiments nor has it been reported in the relevant literature [8–12, 17]. Analysis done by Gheno et al. [12] of the aluminum consumption rate caused by Al_2O_3-Ca_xAl_yO formation during CaO-induced corrosion shows that the extent of aluminum consumption from the alloy subsurface is required to sustain the growth of the Al_2O_3-Ca_xAl_yO would be greater than that required to sustain typical Al_2O_3 growth. Greater subsurface depletion of Al would make the alloy susceptible to internal oxidation when exposed to conditions that favor internal oxidation in the kinetic competition between internal and external oxidation.

CaSO$_4$ Interaction

A representative cross-sectional image of the reaction product formed on coupons deposited with $20 \pm 1 \frac{mg}{cm^2}$ of $CaSO_4$ and exposed for 100 h at 900 °C in air is shown in Fig. 10. A continuous Al-rich scale formed on the surface of the alloy. EDS measurements of the scale detected small amounts of calcium, which suggested that there was limited interaction between the thermally grown aluminum oxide and the
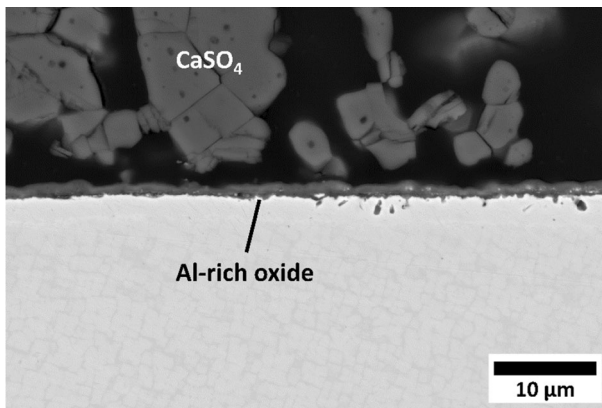

Fig. 10 Reaction product formed on coupons exposed with $20 \pm 1 \frac{mg}{cm^2}$ of $CaSO_4$ for 100 h at 900 °C
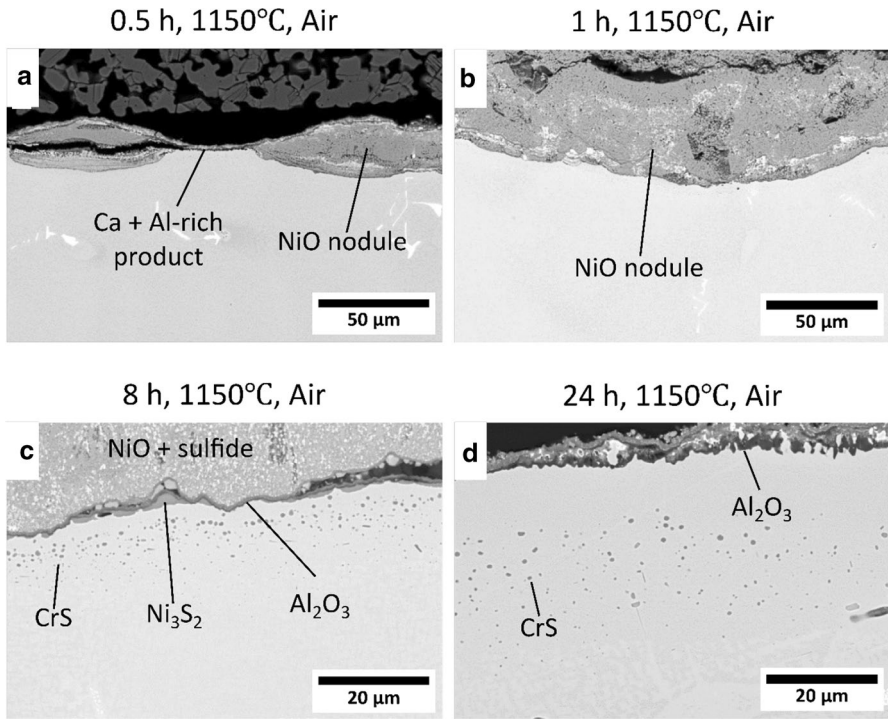
Fig. 11 Reaction product formed on coupons exposed with 20 $\frac{mg}{cm^2}$ of $CaSO_4$ for 0.5 (**a**), 1 (**b**), 8 (**c**), and 24 h (**d**) at 1150 °C in air
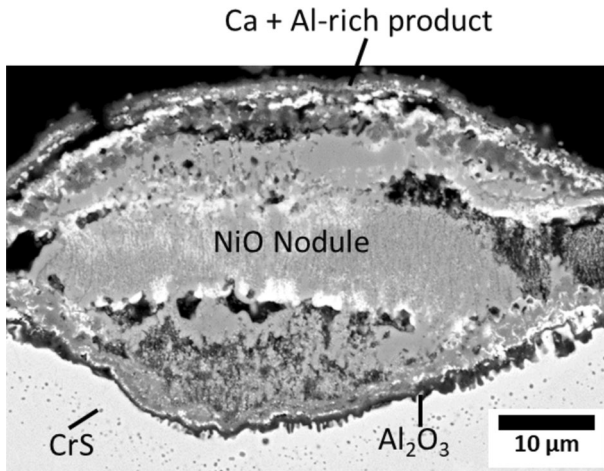

Fig. 12 NiO nodule formed on coupons after 0.5 h of exposure at 1150 °C with $CaSO_4$ deposit

deposit at 900 °C. The lack of corrosion at 900 °C was attributed to low reaction kinetics between $CaSO_4$ and the thermally-grown oxides at this temperature.

Cross-sectional images of the reaction product formed on coupons deposited with $20 \pm 1 \frac{mg}{cm^2}$ of $CaSO_4$ and exposed to air for 0.5, 1, 8, and 24 h at 1150 °C are shown in Fig. 11. After 0.5 h of exposure, an external layer of Al- and Ca-rich reaction product containing 1–2 at% S was present on the coupon surface along with several large NiO nodules. Figure 12 presents a higher magnification image of a NiO nodule on the surface of the alloy after 0.5 h exposure. There was a distribution of CrS particles in the γ' denuded zone beneath the oxide layer similar to that observed in the field-exposed components. Because the only source of sulfur in the experiment was $CaSO_4$, it must have been the interaction between $CaSO_4$ and the coupon that injected sulfur into the alloy. The corrosion morphology after 1 h of exposure is very similar to that after 0.5 h; although, the number and size of the NiO nodules were larger compared to the 0.5 h exposure. After 8 h exposure, the NiO nodules coalesced to form a relatively uniform external nickel-rich reaction product. The external product contained sulfur in addition to oxygen, which suggests co-formation of NiO and nickel sulfide. In most areas, a thin layer of aluminum-rich oxide was present at the base of the nickel-rich product. The distribution of CrS particles in the γ'-denuded zone was still present after 8 h and, occasionally, Ni_3S_2 (inferred on the basis of EDS results) was observed below the Al-rich oxide layer. The corrosion morphology in the coupon exposed for 24 h was similar to that observed after 8 h. The extents of Al and Cr depletion in the coupon subsurface after the 24 h exposure was estimated by EDS. The subsurface aluminum content dropped from the nominal bulk amount of 13.9 at% to 6.5 at% on average and the subsurface chromium content dropped from 6.9 at% to 3.7 at% on average.

In previous descriptions of $CaSO_4$-induced corrosion in electricity-generating power plants [7, 8], sulfidation caused by $CaSO_4$ was attributed to the decomposition of $CaSO_4$ to CaO and SO_3 in areas near the deposit-alloy interface caused by local reducing conditions. In that proposed mechanism, the sulfur potential established by $CaSO_4$ decomposition was shown to be sufficient to form chromium and nickel sulfides in the alloy. The released CaO would then be free to react with thermally grown Al_2O_3 or Cr_2O_3 to form non-protective reaction products [8]. However, this explanation doesn't sufficiently explain the corrosion observed in the present experiments because the decomposition of $CaSO_4$ to CaO and SO_3 has been shown to be very sluggish [18, 19]; while sulfidation and oxide scale breakdown in the present experiments occurred in under 30 min.

$CaSO_4$-Al_2O_3 Interaction

A more comprehensive understanding of the interactions that take place between $CaSO_4$ and Al_2O_3 at 1150°C was gained by placing $20 \frac{mg}{cm^2}$ of $CaSO_4$ on bulk Al_2O_3 and then exposing for 0.5, 8, or 24 h at 1150 °C in air. Subsequent characterization of the reaction product by XRD and EDS after removal of the remnant $CaSO_4$ deposit showed that the reaction product consisted of $Ca_4Al_6O_{16}S$ and $CaAl_2O_4$. Representative XRD spectra from the reaction product after 0.5, 8, and 24 h are shown in
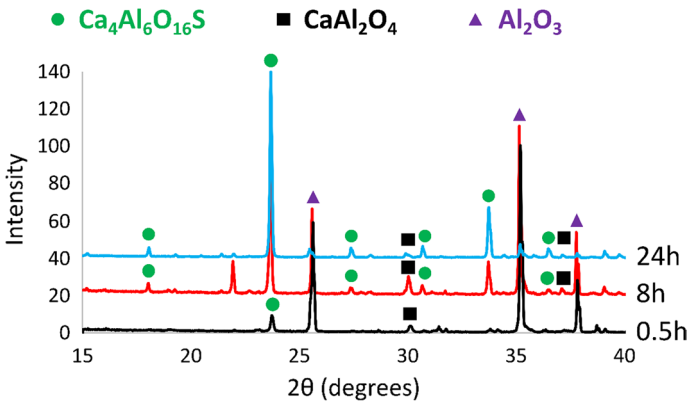
Fig. 13 XRD analysis of reaction product formed between $CaSO_4$ and Al_2O_3 at 1150 °C in air. The reaction product contains $Ca_4Al_6O_{16}S$ and $CaAl_2O_4$
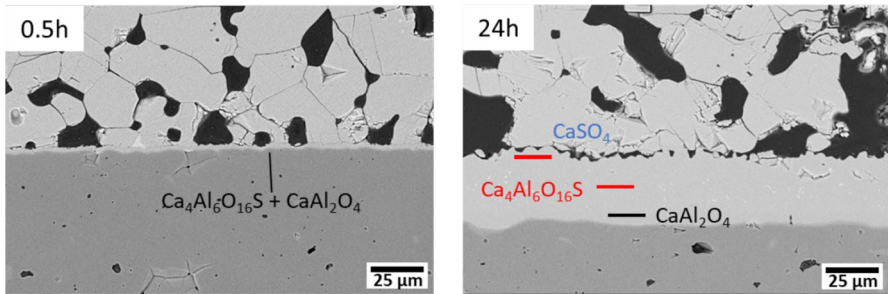

Fig. 14 Reaction product formed between $CaSO_4$-Al_2O_3 coupons exposed for 0.5 h and 24 h at 1150 °C in air as determined by EDS analysis. The bars show areas where EDS was done in the reaction product
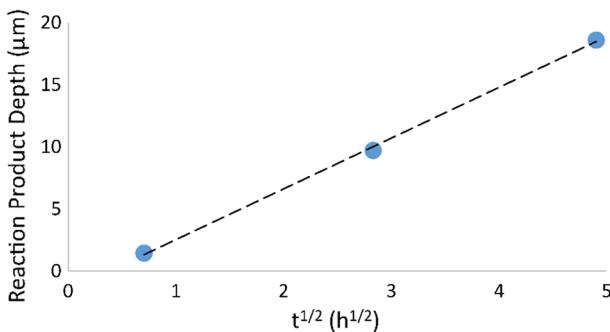

Fig. 15 Parabolic plot of $Ca_4Al_6O_{16}S$ / $CaAl_2O_4$ growth at 1150 °C

Fig. 13. Micrographs of the coupons exposed for 0.5and 24 h are shown in Fig. 14. No CaO or Al was detected in the remnant deposit after any of the exposures, which

suggests that the product grew by solid-state reaction between $CaSO_4$ and Al_2O_3 via inward transport of Ca, O and S through the $Ca_4Al_6O_{16}S$ / $CaAl_2O_4$ layers. The inward transport of Ca and O through calcium aluminate layers is consistent with previous observations [12].

Recording the thickness of the reaction product as a function of $t^{0.5}$ shows that the $Ca_4Al_6O_{16}S$ / $CaAl_2O_4$ layers thickened according to diffusion-controlled parabolic kinetics with a rate constant of $k_p = 4.6 \times 10^{-11} \frac{cm^2}{s}$ at 1150 °C (Fig. 15). Gheno measured the parabolic rate constant for the growth of calcium aluminate caused by CaO-induced corrosion of MCrAlY coatings at 1100 °C to be $k_p = 8.0 \times 10^{-13} \frac{cm^2}{s}$ [12]. The activation energy required to satisfy $k_p = 8.0 \times 10^{-13} \frac{cm^2}{s}$ at 1100 °C and $k_p = 4.6 \times 10^{-11} \frac{cm^2}{s}$ at 1150 °C would be $1316 \frac{kJ}{mol}$. Mohamed et al. [20] estimated the activation energy of calcium aluminate growth to be 204 $\frac{kJ}{mol}$. Therefore, the kinetics of the $Ca_4Al_6O_{16}S$ / $CaAl_2O_4$ growth are significantly faster than calcium aluminate growth.

In accordance with the oxide maps for the Ni–Cr-Al system that were measured by Giggins and Pettit [16], the depletion of Al and Cr from a nickel-based alloy makes it more susceptible to internal oxidation. However, despite significant Al and Cr depletion caused by CaO- and $CaSO_4$-induced corrosion during isothermal exposure in air, no internal attack was observed in any of the test coupons. Therefore, it is inferred that the service environment plays a large role in causing the internal attack observed in the field-exposed components.

Insight into the transition between external and internal oxidation can be gained by considering the fundamental treatment for this transition published by Wagner [21] and reviewed in [22]. Based on that treatment. the critical content of Al in the alloy, N_{Al}^*, for the transition from internal to external Al_2O_3 formation is given by,

$$N_{Al}^* = \left[\frac{\pi g^*}{3} N_O^{(S)} \frac{D_O V_m}{D_{Al} V_{Al_2O_3}} \right] \tag{1}$$

where, g^* is the critical volume fraction of internal Al_2O_3 precipitate to block inward oxygen diffusion and favor lateral Al_2O_3 growth, $N_O^{(S)}$ is the oxygen solubility in the
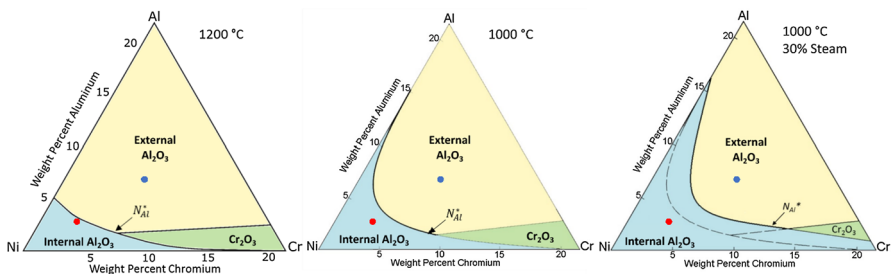

Fig. 16 Oxide maps of NiCrAl adapted from [16, 25] that show how lower temperatures and the presence of water vapor in the atmosphere shift the kinetic boundary between internal and external oxidation to promote internal oxidation

alloy, D_O and D_{Al} are the diffusivities of O and Al in the alloy and V_m and $V_{Al_2O_3}$ are the molar volumes of the alloy and Al_2O_3.

The activation energy for the diffusion of O in Ni [23] is less than activation energy for the diffusion of Al in Ni [24]. Because of this difference, the ratio $\frac{D_O}{D_{Al}}$ in Eq. 1 and hence N_{Al}^* increase as temperature decreases [16]. The presence of water vapor in the atmosphere also tends to increase N_{Al}^* for Ni-based alloys (i.e., water vapor promotes internal Al_2O_3 formation). Based on a systematic study using model Ni-Cr-Al alloys, Zhao and Gleeson [25] deduced that the observed water vapor effect was due to an increase in g^*. The influence of temperature and the presence of water vapor on the kinetic boundary between internal and external oxidation in NiCrAl alloys can be more easily visualized in the oxide maps adapted from [16, 16] presented in Fig. 16 and explained in the following.

Oxide maps show, based on empirical data, what oxide is expected to form on a given bulk alloy composition in the NiCrAl compositional space. In Fig. 16, the composition of the depleted subsurface in N500 after reaction with $CaSO_4$ and measured by EDS is marked with a red dot and the nominal composition of N500 is marked with a blue dot. The maps show that decreasing the exposure temperature and adding steam to the environment shifts the kinetic boundary for Al_2O_3 formation to higher Al and Cr concentrations. This shift with temperature and steam content results in the composition of the depleted subsurface in the alloys reacted with $CaSO_4$ to lie deep enough in the internal oxidation compositional space that the supply of Al from the unaffected bulk alloy to the oxidation front via diffusion may not be sufficient to sustain Al_2O_3 growth. The critical conditions where N500 attacked by $CaSO_4$ begin to internally oxidize were investigated further in [26].

Based on these considerations, a lab-scale experiment, which better simulates service exposure conditions was developed to test the influence that the service environment may have on the development of CaO- and $CaSO_4$-induced corrosion.

Bi-thermal Experimental Design to Replicate Internal Oxidation in Field-exposed Components

The thermal profile shown in Fig. 17 was designed based on the sequence of temperatures that high-pressure turbine components are exposed to during a flight. It
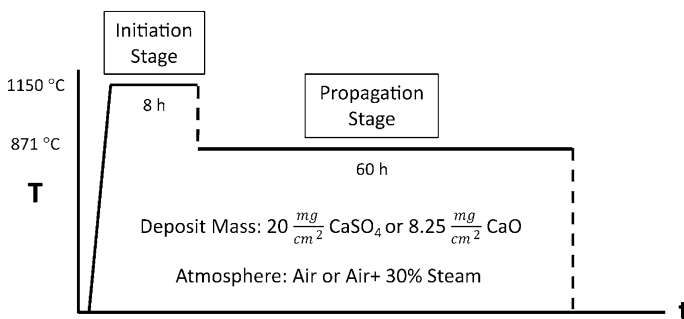

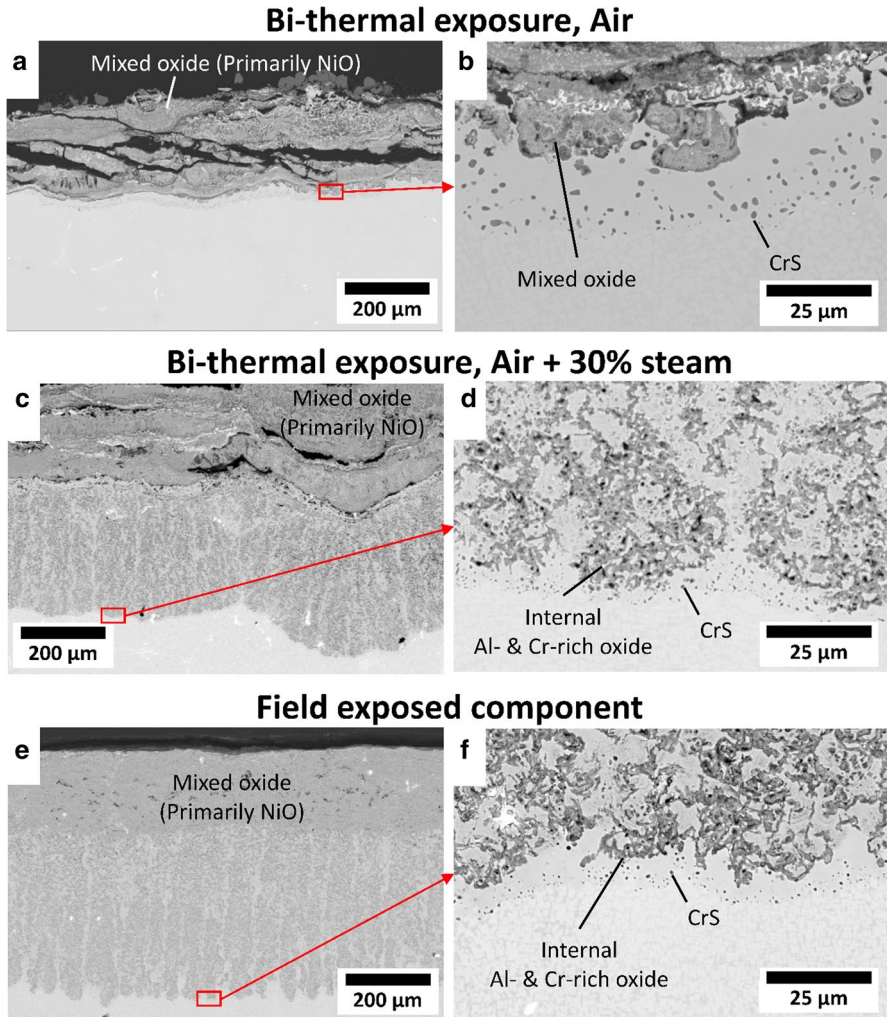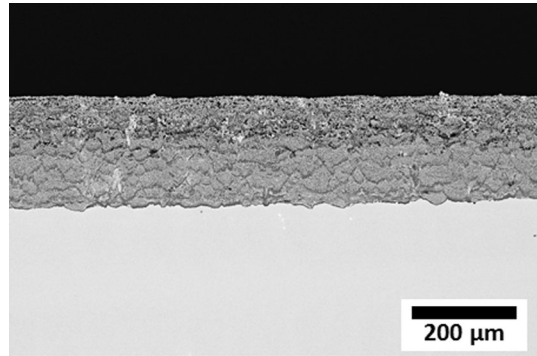**Fig. 17** Bi-thermal testing procedure

Bi-thermal exposure, Air

Bi-thermal exposure, Air + 30% steam

Field exposed component

Fig. 18 Cross-sectional images of coupons after bi-thermal exposures in air (a and b) and air + 30% steam (c and d) with $CaSO_4$ compared to images of a field-exposed component (e and f)

includes an initial exposure at 1150 °C which is representative of the temperature experienced during the takeoff and climb stages of a flight. Based on the results presented so far, it is during this step in the procedure where CaO- and $CaSO_4$-induced corrosion will cause subsurface depletion of Al in the alloy through rapid oxidation and the depletion of Cr due to sulfidation in the case of $CaSO_4$ deposit. This initial step is followed by an exposure at 871 °C (1600°F) which is representative of the temperatures experienced by the component in question during the cruise stage of a flight. It is during the lower temperature exposure where, based on the analysis from Eq. (1), the kinetic competition between external Al_2O_3 growth and internal oxidation of Al is more favorable for internal oxidation.

Coupons with $20 \pm 1 \frac{mg}{cm^2}$ of $CaSO_4$ deposit or $8.25 \pm 0.5 \frac{mg}{cm^2}$ of CaO deposit (an equimolar mass of $CaSO_4$ and CaO deposit) were exposed to the bi-thermal temperature profile in an atmosphere of air or air + 30% steam. Cross-sectional images of coupons with $CaSO_4$ deposit after bi-thermal exposure in air and air + 30% steam are compared to images from a field-exposed component in Fig. 18. A cross-sectional image of the coupon with CaO deposit after exposure in air + 30% steam is shown in Fig. 19.

The coupon with $CaSO_4$ deposit exposed to air with no steam exhibited a thick external mixed oxide layer and subsurface CrS particles. However, internal oxidation like that seen in the field-exposed components was not observed. The morphology of the reaction product present in the coupon with $CaSO_4$ deposit exposed to air + 30% water vapor exhibited the same characteristic features identified in the field-exposed components. Both samples featured a thick external mixed oxide layer consisting of primarily NiO, a deep internal oxidation zone containing coarse Al- and Cr-rich oxide precipitates, and a distribution of fine CrS particles in the γ′-denuded zone ahead of the internal oxidation front. The corrosion product that formed on the coupon with CaO deposit after the bi-thermal test in air + 30% steam has the same morphology seen after CaO-induced corrosion during isothermal exposure at 1150 °C (*cf.* Fig. 8). The reaction product was an adherent layer consisting primarily of mixed Ni, Co, Al, and Cr oxides with bands of calcium aluminate. No significant internal oxidation was observed.

A time study was conducted to determine how the corrosion develops during the bi-thermal exposure with $CaSO_4$ deposit in air + 30% steam. This was done by conducting additional experiments and stopping the tests at three different points during the bi-thermal exposure. Figure 20 summarizes observations of the corrosion at the following stages: a) after the 8 h 1150 °C initiation stage; b) after 1 h at the propagation-stage temperature of 871 °C; and c) after 96 h at the propagation-stage temperature of the 871 °C. After the 8-h initiation stage, $CaSO_4$-induced corrosion caused the subsurface depletion of Al and Cr and enrichment of S in the alloy subsurface. After 1 h at the propagation-stage temperature of 871 °C, there are areas on the alloy where internal oxide precipitates rich in Al and Cr had formed in the alloy subsurface. CrS precipitates were present ahead of the internal oxidation front.
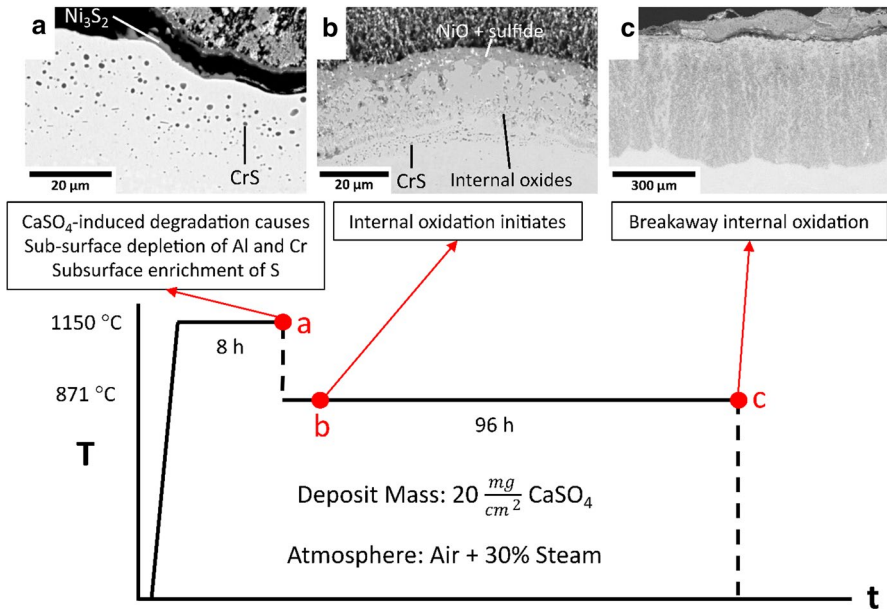
After the full 96-h propagation stage, breakaway internal oxidation and sulfidation had occurred.

The stages of corrosion observed in the time study confirm that the breakaway internal attack is facilitated by the subsurface composition changes caused by CaSO$_4$-induced corrosion at high temperatures. Internal oxidation then initiates and propagates at low-intermediate temperatures in environments containing water vapor because these conditions are more favorable for internal oxidation. The similarities between the corrosion present in the coupons exposed to the bi-thermal test in air + 30% steam and in the field-exposed components indicate that CaSO$_4$-induced corrosion exposed to the bi-thermal test procedure in air + 30% steam accurately reproduces the mechanism of corrosion that took place in the field-exposed components.

The absence of internal attack in the coupon exposed in air + 30% steam with CaO deposit raised questions about the role that subsurface sulfur enrichment plays in the initiation and propagation of the observed internal attack. The role of sulfur was investigated further by comparing a control bi-thermal test with CaSO$_4$ deposit to a similar test where the alloy was de-sulfurized after the 8-h initiation stage at 1150 °C.

Two coupons with 20 $\frac{mg}{cm^2}$ of CaSO$_4$ deposit were exposed for 8 h at 1150 °C in air + 30% steam. Following the initial exposure, the surfaces of both coupons were grit blasted with alumina to remove any external reaction product and one coupon was de-sulfurized using a 24 h exposure at 1000 °C in Ar + 5% H$_2$. After the test coupon was de-sulfurized, both the test and control coupons were subjected to the 60-h propagation
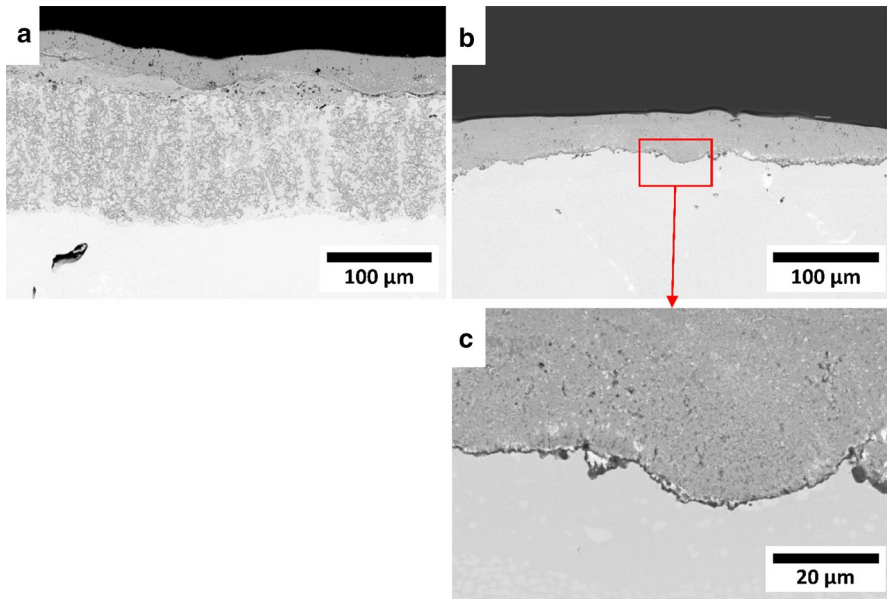
Fig. 21 Cross-sectional micrographs of control bi-thermal test coupon (**a**) and the coupon which was de-sulfidized prior to the propagation stage (**b** and **c**)

stage exposure at 871 °C in air+30% steam. Micrographs of the corrosion product formed on both coupons are shown in Fig. 21. The corrosion product formed on the control coupon (i.e., not desulfurized) consisted of an external layer of NiO above an internal oxidation zone made of Al- and Cr- rich oxides. The morphology of the internal oxidation zone was similar to that seen in the field-exposed components. NiO had also formed on the de-sulfurized coupon but an Al-rich scale was present at the scale-alloy interface, meaning that no internal oxidation was observed in the de-sulfurized coupon. This result suggests that sulfur, even at a very low level, plays a role in promoting internal oxidation in an otherwise similarly depleted alloy subsurface.

Thus, it is inferred that sulfur enrichment in the depleted alloy subsurface is necessary for internal attack to initiate and propagate in coupons that have been subjected to deposit-induced corrosion. This finding is consistent with the work of several other researchers who have found that subsurface sulfidation is detrimental to the ability of Ni-based alloys to establish a protective oxide layer [27–29]. While the precise mechanisms by which sulfur promotes internal attack during bithermal testing are unknown, it is likely that one underlying cause is CrS formation ahead of the internal oxidation front resulting in significant Cr depletion from the alloy matrix. Such a form of Cr depletion is a self-sustaining process that persists at the internal oxidation front as it progresses. Spengler et al. [29] and Meijering [30] describe the process by which sulfur is continuously injected deeper into the alloy as the oxidation front progresses. Cr_2O_3 is more thermodynamically

stable than CrS so, as the P_{O_2} ahead of the internal oxidation front increases, the CrS precipitates are oxidized to form Cr_2O_3. The sulfur released by the oxidation of CrS particles then diffuses deeper into the alloy where the sulfur and oxygen activity are low and the chromium activity is high. The sulfur then reacts with Cr to form new CrS particles, maintaining the depletion of Cr from the alloy matrix at the oxidation front. With such a Cr depletion, the Al that remains in the matrix is ostensibly below N_{Al}^* (Eq. 1). Further research is necessary to determine possible other mechanisms by which subsurface sulfur enrichment can promote the internal oxidation process during bi-thermal exposure.

Conclusions

The present research has demonstrated that CaO and $CaSO_4$ can cause corrosion of nickel-based superalloys through solid-state reaction between the deposit and thermally grown oxides to form non-protective reaction products. Additionally, further investigation of $CaSO_4$-induced corrosion led to the development of a bi-thermal test procedure, which accurately reproduces internal oxidation and sulfidation observed in field-exposed components. The greater understanding of the modes of corrosion that occur in the field gained by an accurate lab-scale test procedure makes it an invaluable tool that can inform material development. This replication procedure can be used to develop more effective mitigation strategies against modes of attack that current components are exposed to during service and can allow researchers to evaluate future materials more accurately for gas-turbine applications.

It was found that the mode of corrosion in the field-exposed components is breakaway internal oxidation-sulfidation initiated by $CaSO_4$-induced corrosion. The depletion of aluminum and chromium from the alloy subsurface caused by $CaSO_4$-induced corrosion at 1150℃ resulted in the alloy becoming susceptible to internal oxidation. When the subsurface-depleted alloy was subsequently exposed to a lower temperature of 871 ℃ in air+30% steam (environmental conditions that promote internal oxidation), breakaway internal oxidation initiated and propagated in a way that closely matched the corrosion in the field-exposed parts. $CaSO_4$-induced internal oxidation and sulfidation will be the subject of subsequent papers based on thesis work [26] which investigated how variables such as time and temperature profile, alloy composition, and deposit composition affect modes of deposit-induced internal attack.

References

1. B. A. Pint, High-temperature corrosion in fossil fuel power generation: present and future. *JOM* **65**, 1024 (2013).

2. D. A. Shifler"The Increasing Complexity of Hot Corrosion," Journal of Engineering Gas Turbines Power, (2017).
3. R. A. Rapp, Hot corrosion of materials: a fluxing mechanism? *Corrosion science* **44**, 209 (2002).
4. G. H. Meier, *Current Aspects of Deposit-Induced Corrosion*, (Springer, USA, 2021).
5. F. Pettit, Hot corrosion of metals and alloys. *Oxidation of Metals* **76**, 1 (2011).
6. M. B. Krisak, B. I. Bentley, A. W. Phelps, and T. C. Radsick, Review of calcium sulfate as an alternative cause of hot corrosion. *Journal of Propulsion and Power* **33**, 697 (2017).
7. T. J. Nijdam and R. van Gestel, Service experience with single crystal superalloys for high pressure turbine shrouds, *Natl. Lucht- en Ruimtevaartlaboratorium*. NLR-TP-2011–547, (2010).
8. J. Stringer and A. J. Minchener, High temperature corrosion in fluidized bed combustion systems. *Journal of materials for energy systems* **7**, 333 (1986).
9. J. Stringer and I. G. Wright, Materials issues in fluidized bed combustion. *Journal of materials for energy systems* **8**, 319 (1986).
10. K. T. Chiang, G. H. Meier, and R. A. Perkins, The effects of deposits of CaO, CaSO4, and MgO on the oxidation of several Cr2O3-forming and Al2O3-forming alloys. *Journal of materials for energy systems* **6**, 71 (1984).
11. K. Jung, "Solid Deposit-Induced High Temperature Oxidation," University of Pittsburgh, 2008.
12. T. Gheno, G. H. Meier, and B. Gleeson, High temperature reaction of MCrAlY coating compositions with CaO deposits. *Oxidation of Metals* **84**, 185–209 (2015).
13. I. Barin, *Thermochemical Data of Pure Substances*, 3rd ed. Wiley, 2008.
14. A. Durga, H. Dai, S. Huang, I. Spinelli, and L. Yuan, Grain structure prediction for directionally solidified superalloy castings. *JOM* **72**, 1785–1793 (2020).
15. C. F. Beaton, *Heat Exchanger Design Handbook*. Hemisphere Publishing Corp, 1986.
16. C. S. Giggins and F. Pettit, Oxidation of Ni-Cr-Al alloys between 1000 and 1200° C. *Journal of the Electrochemical Society* **118**, 1782 (1971).
17. K. Y. Jung, F. S. Pettit, and G. H. Meier, The effect of Ca-rich deposits on the high temperature degradation of coated and uncoated superalloys. *Materials Science Forum*. **595**, 805 (2008).
18. W. M. Swift, A. F. Panek, G. W. Smith, G. J. Vogel, and A. A. Janke, "Decomposition of Calcium Sulfate: a Review of the Literature." pp. 1–64, 1976.
19. I. Colussi and V. Longo, La decomposizione termica del solfato di calcio. *Il Cemento* **2**, 75 (1974).
20. B. M. Mohamed and J. H. Sharp, Kinetics and mechanism of formation of monocalcium aluminate, $CaAl_2O_4$. *Journal of Materials Chemistry* **7**, 1595 (1997).
21. C. Wagner, Reaktionstypen bei der Oxydation von Legierungen. *Zeitschrift für Elektrochemie, Berichte der Bunsengesellschaft für physikalische Chemie* **63**, 772 (1959).
22. N. Birks, G. H. Meier, and F. S. Pettit, *Introduction To The High Temperature Oxidation of Metals*, 2nd ed. Cambridge University Press, 2006.
23. J. W. Park and C. J. Altstetter, The diffusion and solubility of oxygen in solid nickel. *Metallurgical Transactions A* **18**, 43 (1987).
24. M. S. A. Karunaratne, P. Carter, and R. C. Reed, On the diffusion of aluminium and titanium in the Ni-rich Ni–Al–Ti system between 900 and 1200 C. *Acta materialia* **49**, 861 (2001).
25. W. Zhao and B. Gleeson, Assessment of the detrimental effects of Steam on Al2O3-scale establishment. *Oxidation of Metals* **83**, 607 (2015).
26. P. T. Brennan, "Environmental Factors Affecting CaO and CaSO4-Induced Degradation of Second-Generation Nickel-Based Superalloys," University of Pittsburgh, 2020.
27. J. A. Goebel and F. S. Pettit, The influence of sulfides on the oxidation behavior of nickel-base alloys. *Metallurgical Transactions* **1**, 3421 (1970).
28. B. Schramm and W. Auer, Sulfidation behaviour of nickel aluminides. *Material Corrossion* **47**, 678 (1996).
29. C. J. Spengler and R. Viswanathan, Effect of sequential sulfidation and oxidation on the propagation of sulfur in an 85 Ni-15 Cr alloy. *Metallurgical and Materials Transactions B* **3**, 161 (1972).
30. J. L. Meijering, *Advances in Materials Science*. Wiley, 1971.

Publisher's Note Springer Nature remains neutral with regard to jurisdictional claims in published maps and institutional affiliations.